

Space-time characterization of ultra-intense femtosecond laser beams

G. Pariente¹, V. Gallet¹, A. Borot^{1,2}, O. Gobert¹ and F. Quéré^{1*}

Femtosecond lasers can now deliver ultrahigh intensities at focus, making it possible to induce relativistic motion of charged particles with light and opening the way to new generations of compact particle accelerators and X-ray sources. With diameters of up to tens of centimetres, ultra-intense laser beams tend to suffer from spatiotemporal distortions, that is, a spatial dependence of their temporal properties that can dramatically reduce their peak intensities. At present, however, these intense electromagnetic fields are characterized and optimized in space and time separately. Here, we present the first complete spatiotemporal experimental reconstruction of the field $E(t,r)$ for a 100 TW peak-power laser, and reveal the spatiotemporal distortions that can affect such beams. This new measurement capability opens the way to in-depth characterization and optimization of ultra-intense lasers and ultimately to the advanced control of relativistic motion of matter with femtosecond laser beams structured in space-time.

One of the major achievements of optics in recent decades has been the generation of light pulses of extremely short duration, down to a few femtoseconds in the 1990s^{1,2} and tens of attoseconds in the past few years^{3,4}. Such ultrashort pulses can be used to temporally resolve the ultrafast dynamics of excited matter in pump-probe experiments. Furthermore, when amplified to energies in the Joule range in ultrahigh-intensity (UHI) lasers, femtosecond pulses make it possible to expose matter to considerable light intensities, such that the motion of electrons in the laser field is relativistic⁵.

Throughout the development of these sources, the ability to accurately measure the temporal properties of ultrashort light pulses has been crucial. Several well-established techniques are now available to measure their electric field $E(t)$ from the femtosecond^{6,7} down to the attosecond range⁸. However, within any ultrashort beam, the temporal properties of the light pulse can vary spatially^{9,10} and vice versa. Such correlations between the spatial and temporal properties are called spatiotemporal couplings (STCs) and prevent the decomposition of the laser field $E(t,r)$ as $E(t,r) = f(t)g(r)$. A simple Fourier transform with respect to time shows that STCs are the temporal counterpart of conventional chromatism, that is, the frequency dependence of the spatial properties of a light beam.

STCs are ubiquitous in ultrafast optics. They tend to naturally affect current attosecond light sources, where they are either induced directly by the highly nonlinear generation process¹¹ or by aberrations of the optical systems used to manipulate them¹². In the femtosecond range, chirped-pulse amplification (CPA), the key technology of amplified ultrashort pulses¹³, relies on the use of massive STCs induced at different locations in laser systems (for instance by gratings or prisms), which should all eventually perfectly cancel out at the laser output. Residual STCs, for example resulting from imperfect compensation, decrease the peak intensity at focus by increasing both the focal spot size and the pulse duration⁹. This is particularly detrimental for UHI lasers, which aim for the highest possible peak intensities. However, it is precisely with these lasers that such uncontrolled defects are most likely to occur, due to the complexity of these systems and the large diameters of the output beams.

Accurately measuring STCs is thus essential in ultrafast optics. Significant progress has been made in the last decade, and several techniques are now available for the partial or complete spatiotemporal characterization of near-visible femtosecond laser beams (see, for example, refs 14–21). However, none of these has yet been applied to UHI femtosecond lasers, due to the difficulty of handling these large and powerful beams. As a result, all UHI lasers are currently characterized under the unjustified and unverified assumption of the absence of STCs, using separate measurements in space (for example, by imaging or wavefront sensing) and time (by measurements of $E(t)$ at one given location in the beam). This situation is now becoming a major bottleneck for the development of UHI lasers and their applications. In particular, the optimal and reliable operation of PW-class lasers now available or under construction all around the world^{22–25} will simply not be possible without a proper spatiotemporal metrology. In this Article, we demonstrate the first complete spatiotemporal reconstruction of a 100 TW class UHI laser, using a measurement scheme derived from the recently developed technique of spatially resolved Fourier-transform spectroscopy^{26,27}.

A bird's eye view of STCs

We first briefly introduce the key ideas behind STCs, and more particularly about their metrology and their impact on the performances of femtosecond lasers. The laser field $E(t,r)$ can equivalently be described in the frequency domain by its spatially resolved complex spectrum $\tilde{E}(\omega, \mathbf{r}) = A(\omega, \mathbf{r})e^{i\phi(\omega, \mathbf{r})}$, where $A(\omega, \mathbf{r})$ and $\phi(\omega, \mathbf{r})$ are, respectively, the spatio spectral amplitude and phase. $A(\omega, \mathbf{r})$ can be measured easily for beams of arbitrary diameter, for example, by scanning this beam with a fibre-coupled spectrometer. The main difficulty for the spatiotemporal characterization of ultrashort beams is related to the measurement of $\phi(\omega, \mathbf{r})$.

To explain the crucial effects of this phase on an ultrashort laser beam, we use a Taylor expansion with respect to frequency, around the central frequency ω_0 of the pulse:

$$\phi(\omega, \mathbf{r}) = \phi(\omega_0, \mathbf{r}) + \frac{\partial \phi(\omega_0, \mathbf{r})}{\partial \omega} \delta\omega + \phi(\omega, \mathbf{r}) \quad (1)$$

¹LIDYL, CEA, CNRS, Université Paris-Saclay, CEA Saclay, 91 191 Gif-sur-Yvette, France. ²Max-Planck-Institut für Quantenoptik, D-85748 Garching, Germany.
*e-mail: fabien.quere@cea.fr

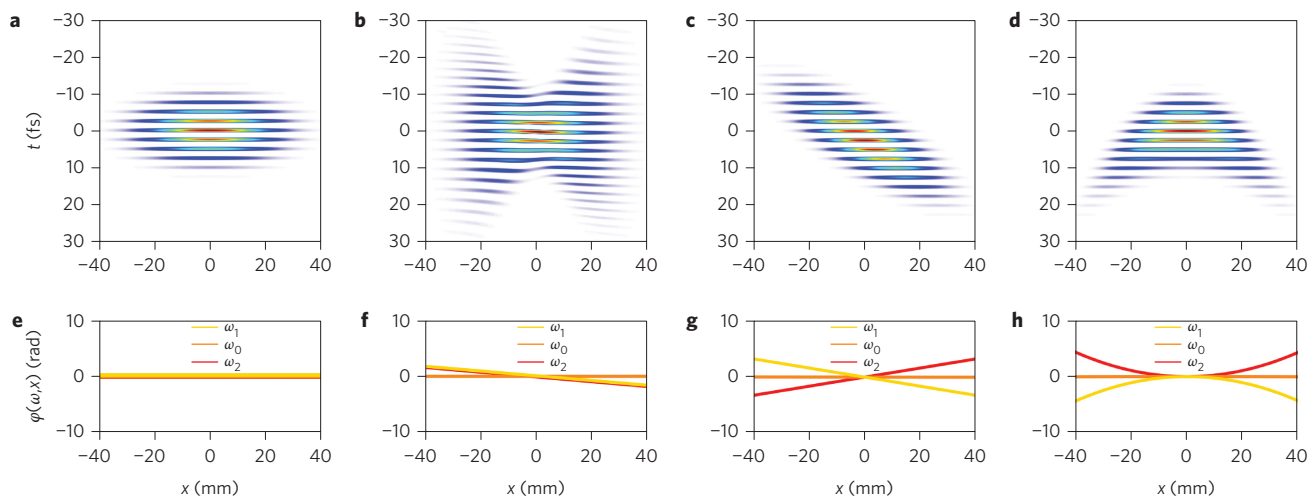


Figure 1 | Examples of collimated femtosecond laser beams with different STCs. **a-d**, Theoretical examples of the field E of a femtosecond laser beam in two-dimensional space (x, t): perfect Gaussian beam (in space and time) without any STC (**a**); beam with a radially increasing group delay dispersion, $\varphi(\omega, x) = \phi(\omega, x) \propto x \delta\omega^2$ (**b**); beam with PFT, $\varphi(\omega, x) = \xi x \delta\omega$ (**c**); beam with PFC, $\varphi(\omega, x) = \alpha x^2 \delta\omega$ (**d**). **e-h**, For each case, the spatial phase profile for three different frequencies $\omega_1 < \omega_0 < \omega_2$ of the pulse, showing how the field wavefronts depend on frequency in the presence of different STCs. According to the previous expressions of $\varphi(\omega, x)$, the wavefront tilt varies quadratically with frequency in case **b** (**f**), and linearly in case **c** (**g**). In case **d**, it is now the wavefront curvature that varies linearly with ω (**h**).

where $\delta\omega = \omega - \omega_0$ and where $\phi(\omega, \mathbf{r})$ includes all terms of the Taylor expansion of order higher than 1 in $\delta\omega$. This last term accounts for the temporal shape of the light pulse and its possible variations across the beam, due for instance to a spatially varying linear group delay dispersion, $\phi(\omega, \mathbf{r}) = f(\mathbf{r})\delta\omega^2$ (Fig. 1a,b). In principle, it can be determined by performing measurements of the pulse shape at different positions in the beam, using one of the techniques developed for temporal metrology of ultrashort pulses²⁸. However, such a set of measurements is far from sufficient for a complete knowledge of the field in space–time due to the first two terms on the right side of equation (1).

The first term, $\varphi_0(\mathbf{r}) = \varphi(\omega_0, \mathbf{r})$, describes the phase profile of the beam at the central frequency ω_0 (orange lines in Fig. 1e-h). The three-dimensional surface $\Sigma = (\mathbf{r}, z = \varphi_0(r)/k_0)$, with $k_0 = \omega_0/c$, is the wavefront of the beam at this frequency. In the second term, $\tau_0(\mathbf{r}) = \partial\varphi(\omega_0, \mathbf{r})/\partial\omega$ has the dimension of time: it is the local group delay of the pulse, and determines the arrival time of the light pulse at position \mathbf{r} . The three-dimensional surface $\Pi = (\mathbf{r}, z = c\tau_0(\mathbf{r}))$ is called the pulse front of the beam. Intuitively speaking and to first order in frequency, it describes the location of the light beam energy in space–time.

Differences between the beam wavefront Σ and its pulse front Π correspond to a category of STC known as pulse front distortions (Fig. 1c,d). These correspond to cases where the arrival time of the light pulse varies with the transverse coordinate, with respect to the reference wavefront Σ . These can alternatively be viewed as spatial variations of the carrier-envelope relative phase (CEP) of the pulse across the beam. As shown by equation (1), these are the STCs of lowest order in $\delta\omega$ and are therefore often expected to be predominant in femtosecond laser beams. Measuring such distortions requires a technique that is sensitive to spatial variations not only of the duration, but also of the phase and arrival time of the light pulse. This is what makes the problem of STC metrology far more difficult than simply measuring the pulse envelope shape as a function of position.

To illustrate these concepts, Fig. 1c,d shows two of the simplest STCs commonly expected on collimated beams at the output of femtosecond lasers, which both correspond to pulse front distortions. Figure 1c shows a beam with pulse front tilt (PFT)²⁹, which is a linear offset between the laser wavefront and pulse front, that is, $\tau_0(x) = \xi x$ (assuming $\varphi_0(\omega_0, \mathbf{r}) = 0$ for simplicity), where ξ is the

PFT parameter, generally expressed in fs mm^{-1} . A PFT can be induced by any angularly dispersive optical element³⁰. In CPA lasers, such dispersive elements are used for control of the pulse duration¹ and are ideally arranged in such a way that the different PFTs individually induced eventually cancel out, although misalignment typically leads to a residual PFT. Figure 1d shows a beam with pulse front curvature (PFC), which corresponds to different curvatures of the wavefront and pulse front, that is, $\tau_0(x) = \alpha x^2$ (again assuming $\varphi_0(\omega_0, \mathbf{r}) = 0$), where α is the PFC parameter, generally expressed in fs mm^{-2} . PFC is typically induced by chromatic lenses³¹.

As already mentioned, the counterpart of STCs in the frequency domain is a dependence on ω of the spatial properties of the beam. In many cases, such as those displayed in Fig. 1b-d, this dependence consists in a variation of the light wavefronts with frequency, as illustrated in Fig. 1f-h. Consequently, when focusing a beam with such STCs, the different frequencies making up the laser pulse are focused at different positions, transversely (for the case of PFT, see Fig. 2a) and/or longitudinally (for PFC, see Fig. 2b). This increases the size of the integrated focal spot of the focused beam and reduces the local spectral bandwidth, thus potentially increasing the pulse duration. The reduction in peak intensity at focus resulting from the combination of these temporal and spatial effects can be dramatic.

This intensity reduction is plotted for the case of PFT and PFC in Fig. 2c,d, respectively, as a function of the strength ξ and α of these couplings, for four combinations of laser beam diameter and pulse duration, typical of lasers of different classes of peak power from the TW to the multi-PW range, either existing or under construction. Cases 1 and 2 typically correspond to TW-class lasers used for the generation of high-order harmonics and attosecond pulses in gases, while cases 3 and 4, respectively, correspond to the 100 TW and 10 PW-class lasers used for laser-driven particle acceleration and relativistic optics. These plots clearly show that for a given STC strength, the intensity reduction becomes all the more dramatic as the pulse duration decreases and as the beam diameter increases.

With their combination of large diameter and ultrashort duration, UHI femtosecond lasers are particularly sensitive to STC. In the case of the APOLLON laser, a 10 PW beam of 400 mm diameter and 15 fs duration now under construction in France, a tenfold

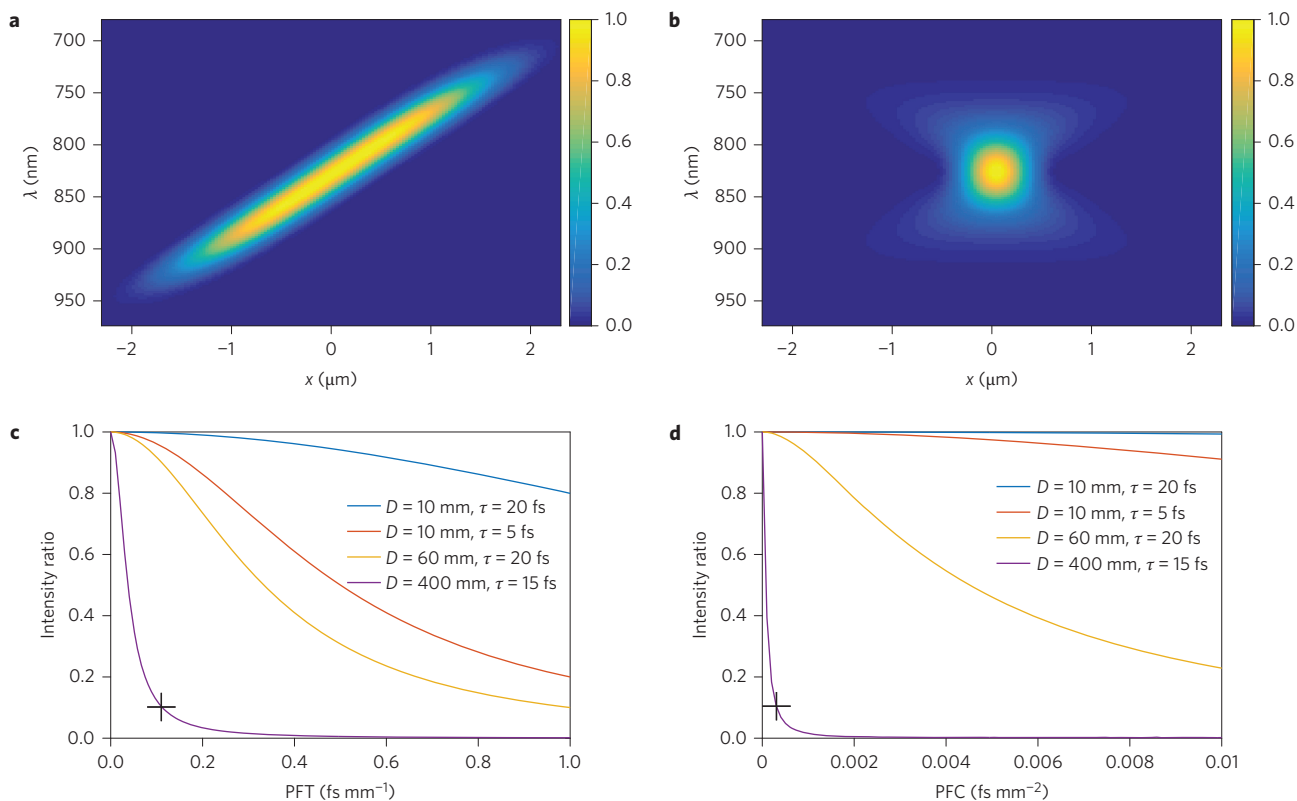


Figure 2 | Consequences of STCs at focus. **a,b**, Spatially resolved spectrum obtained at focus, when focusing initially collimated beams with PFT (**a**) and PFC (**b**). In **a**, the different frequencies are focused at slightly different transverse positions. In the second case, they are focused at different depths z , so that at given z_0 , the size of the beam varies with ω , as in **b**. **c,d**, The resulting reduction in peak intensity at focus, relative to the case of a perfect STC-free Gaussian beam of the same diameter and spectrum, induced by PFT in **a** and PFC in **b**. In both cases, this reduction is calculated as a function of the strength (ξ in **a**, α in **b**) of the STC, for four combinations of pulse duration and beam diameter. The two crosses indicate the cases in **a** and **b** that both correspond to the 10 PW APOLLON laser (15 fs duration, 400 mm diameter).

reduction in peak intensity at focus will occur for a PFT of ~ 0.1 fs mm^{-1} (typically corresponding to a deviation of only ~ 20 μrad in the parallelism of the compressor gratings) or a PFC of 3×10^{-4} fs mm^{-2} . In practice, there are many other possible effects, such as faulty optics or nonlinear effects, that can lead to even more complex STCs on UHI laser beams, and these will generally tend to have stronger impacts on larger beams and shorter pulses. These extreme numbers clearly show that the peak intensity of such lasers cannot be reliably estimated without a complete spatiotemporal characterization.

TERMITES spatiotemporal measurement technique

Here, we use a self-referenced interferometric technique to obtain the first spatiotemporal reconstruction of a UHI laser. The key idea is to use a portion of the unknown laser beam as a reference, and to compare the properties (CEP, group delay and pulse shape) of the laser pulses $E(t,\mathbf{r})$ at all other points of the beam with this reference. This comparison between different points of the beam is achieved using an advanced version of the technique of spatially resolved Fourier-transform spectroscopy, developed independently in Lund and Saclay in the last two years^{26,27}. We refer to this technique as TERMITES, which stands for ‘total E -field reconstruction using a Michelson interferometer temporal scan’. The corresponding measurement device, placed on the collimated and attenuated beam at the laser output, just after the compressor, is sketched in Fig. 3a, and simply consists of a special Michelson interferometer, a diffusive screen and a charge-coupled device (CCD) camera. It avoids complex manipulations of the beam and is thus ideal for the characterization of UHI lasers.

One arm of the interferometer contains a flat mirror, and reflects the unknown beam, of diameter D . The other arm contains a convex mirror that reflects a spatial portion of the beam of diameter $D_R = \beta D$ ($\beta < 1$) and makes it diverge to produce the reference beam. A diffusive screen then intersects the output of this interferometer, scatters the laser light and is imaged on a CCD camera with a standard photographic lens. This screen is placed at a distance from the interferometer large enough for the diameter of the diverging reference beam to exceed that of the unknown beam. Both beams can thus interfere over the entire diameter D of the unknown beam, producing circular interference fringes such as those shown in Fig. 3b. The experimental procedure consists of scanning the delay between the two interferometer’s arms with sub-laser cycle accuracy and recording the image of the spatial interference pattern for each delay.

Through this set of spatially resolved interferences, we can compare the local complex spectra of the two beams by Fourier-transform spectroscopy. Indeed, the interferometric part of the signal at any given point \mathbf{r} corresponds to the local cross-correlation function $s(\tau, \mathbf{r})$ of the unknown and reference beams (Fig. 3c):

$$s(\tau, \mathbf{r}) = \int dt E(t, \mathbf{r}) E_R^*(t - \tau, \mathbf{r}) \quad (2)$$

where $E_R(t, \mathbf{r})$ is the complex field of the reference beam in the measurement plane. By Fourier-transforming $s(\tau, \mathbf{r})$ with respect to the delay τ (Fig. 3d), we obtain the local cross-spectral density $\tilde{s}(\omega, \mathbf{r})$ of the reference and unknown beams:

$$\tilde{s}(\omega, \mathbf{r}) = \tilde{E}(\omega, \mathbf{r}) \tilde{E}_R^*(\omega, \mathbf{r}) = |\tilde{E}(\omega, \mathbf{r}) \tilde{E}_R(\omega, \mathbf{r})| e^{i[\varphi(\omega, \mathbf{r}) - \varphi_R(\omega, \mathbf{r}) - \omega \tau_0(\mathbf{r})]} \quad (3)$$

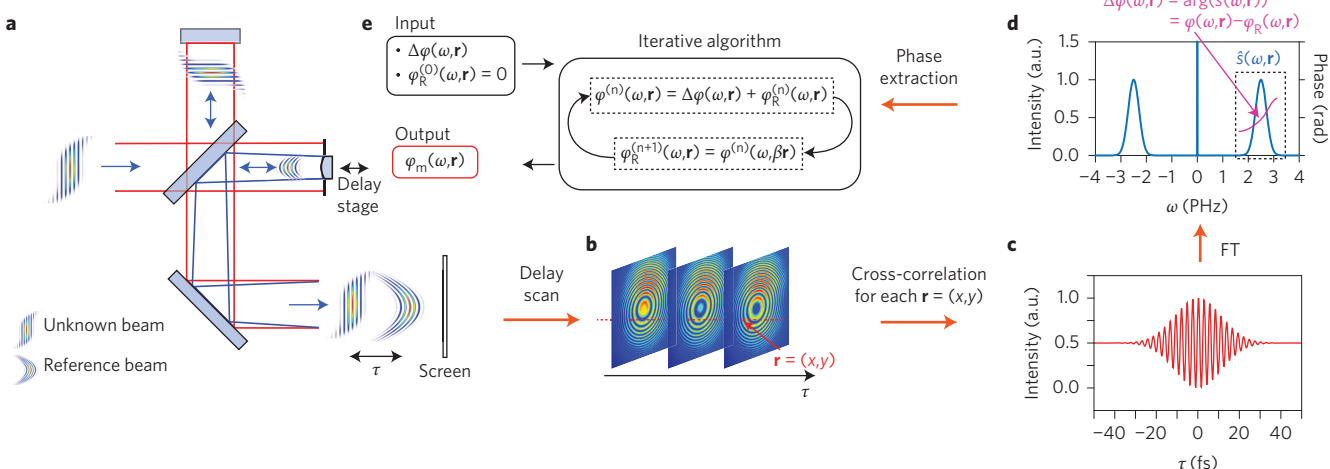


Figure 3 | Principle of the TERMITES spatiotemporal measurement technique. **a**, The measurement device, consisting of an asymmetric Michelson interferometer. **b**, This produces two outgoing beams, which, due to their different divergences, produce an interference pattern consisting of quasi-circular fringes. This interference pattern is measured as a function of the delay between the two beams, scanned with sub-laser period accuracy until extinction of the fringes. **c**, At each pixel of the image, this measurement provides the linear cross-correlation function $s(\tau, \mathbf{r})$ between the unknown and reference beams. **d**, A Fourier analysis of this trace provides the cross-spectral density $\hat{s}(\omega, \mathbf{r})$ of the reference and unknown beams. **e**, From this complex function, we extract the spatio-spectral phase $\varphi(\omega, \mathbf{r})$ of the unknown beam using an iterative algorithm that exploits the fact that the reference is a radially stretched replica of this unknown beam. See Supplementary Information for details on the measurement device and data processing.

where $\tau_0(\mathbf{r}) = \alpha|\mathbf{r}|^2$ is the radially varying delay associated with the spatial curvature of the reference beam (Fig. 3a). Applied to all pixels of the measured images, this data processing thus provides $\Delta\varphi(\omega, \mathbf{r}) = \varphi(\omega, \mathbf{r}) - \varphi_R(\omega, \mathbf{r})$, once the phase $\omega\tau(\mathbf{r})$ associated with the reference curvature has been numerically removed (Supplementary Section II.A.2).

The next step consists in eliminating the reference phase $\varphi_R(\omega, \mathbf{r})$ from $\Delta\varphi(\omega, \mathbf{r})$, to extract the spatio-spectral phase $\varphi(\omega, \mathbf{r})$ of the unknown beam. To this end, we exploit the fact that the reference beam in the measurement plane is a radially-stretched replica of the unknown beam, so that $\varphi_R(\omega, \mathbf{r}) = \varphi(\omega, \beta\mathbf{r})$, and $\Delta\varphi(\omega, \mathbf{r})$ is actually determined solely by $\varphi(\omega, \mathbf{r})$. We deduce this function from $\Delta\varphi(\omega, \mathbf{r})$ using a simple iterative algorithm (Fig. 3e, see Supplementary Section II.A.3 for more details) that initially assumes a perfect reference beam ($\varphi_R^{(0)}(\omega, \mathbf{r}) = 0$) and is repeated until it converges to a retrieved phase $\varphi_{\text{ret}}(\omega, \mathbf{r})$, such that $\Delta\varphi(\omega, \mathbf{r}) = \varphi_{\text{ret}}(\omega, \mathbf{r}) - \varphi_{\text{ret}}(\omega, \beta\mathbf{r})$. Simulations show that in the absence of noise, this algorithm converges to the exact solution, even when the reference covers a very large fraction of the unknown beam (that is, $\beta \rightarrow 1$).

Finally, because this procedure relies on a comparison between different spatial parts of the beam, uniformly applying any spectral phase $\varphi_0(\omega)$ to all points still provides a valid solution. Removing this indeterminacy requires a measurement of the spectral phase $\varphi(\omega, \mathbf{r}_0)$ of the field at any given point \mathbf{r}_0 . In our case, this additional measurement was performed by applying the Wizzler technique³² to a small central part of the beam, as is usually done to check the optimal compression of these lasers. The field reconstruction is finally obtained up to a global phase φ_0 . Apart from this indeterminacy, this set of measurements provides all information on the spatiotemporal structure of the beam, including all types of pulse front distortions, as well as possible spatial variations of the pulse duration or shape.

We have performed a variety of validation tests of the results provided by this measurement technique, which are presented in Supplementary Section III, and have confirmed their validity and accuracy.

Experimental results and discussion

This technique was used to obtain the complete spatiotemporal reconstruction of the E field of an ultra-intense laser, the UHI100

laser at CEA Saclay. This commercial laser has a peak power of 100 TW, a Fourier-transform limited pulse duration of 25 fs and a diameter of $D \approx 65$ mm. The retrieved three-dimensional field $E(t, \mathbf{r})$ of the collimated beam, right at the laser output, is presented in Fig. 4a (see Supplementary Movie 1 for multiple perspectives), together with its projections in the different subspaces. On this plot, the frequency of the carrier wave has been numerically reduced for the sake of visualization. From this representation, the beam does not appear at first sight to suffer from major STC: no large pulse front distortion, such as PFT or PFC, is observed, and the pulse duration is rather homogeneous. Yet, it is clear that the beam is not perfect either. We now show how a much finer and more quantitative analysis of its properties can be carried out.

To this end, we consider the coordinate space (ω, \mathbf{r}) , where the initial field reconstruction is provided by TERMITES and study $\tilde{E}(\omega, \mathbf{r})$ —what might be called a complex hyperspectral image of the beam—with 50 sampling points in frequency and 200×200 sampling points in position. This provides frequency-resolved two-dimensional spatial amplitude and phase maps of the beam, which are displayed in Fig. 4b–g for three different frequencies ω (see Supplementary Movie 2 for the complete evolution as a function of ω). This set of data is similar to what would be obtained by performing measurements with a frequency-resolved wavefront sensing system¹⁹ with an unusually high spatial resolution.

Much finer details on the beam structure now appear on this representation, which would be undetectable with spectrally integrated measurement devices. As far as the amplitude is concerned, our measurements reveal that the left edge of the laser beam becomes increasingly clipped on the ‘blue’ side of the spectrum (Fig. 4b) due to an optical mount in the compressor that intersects the beam when it is spatially chirped. As for the phase profiles, the most striking feature is a sharp crescent-shape phase variation of about 2π in magnitude (Fig. 4f,g) that gradually appears on the ‘red’ side of the spectrum. The location in the beam of this phase distortion drifts linearly with frequency. This frequency dependence indicates that this phase aberration is induced by a faulty optical element again located in the compressor, where the beam is spatially chirped. Apart from this noteworthy distortion, the phase profile is rather smooth and regular at all frequencies. A fine analysis,

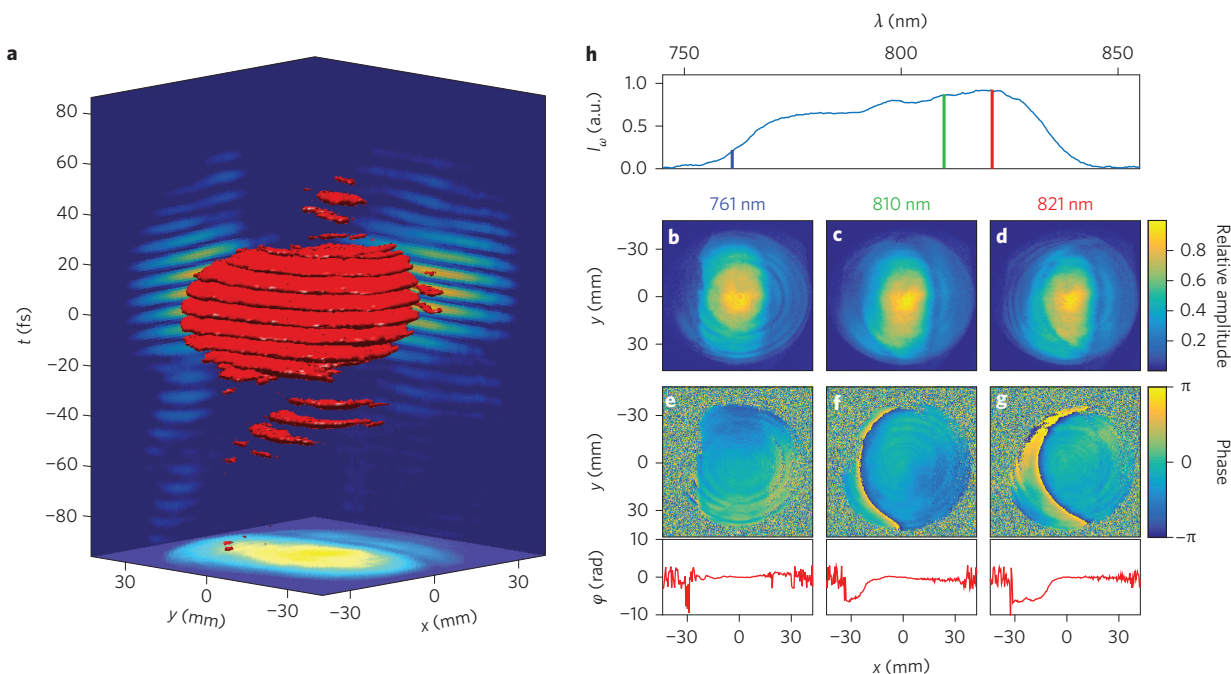


Figure 4 | Complete reconstructions of the E field of a 100 TW laser beam. **a**, E field of the collimated beam at the laser output in space and time (isosurface at 20% of the peak field value). The frequency of the carrier wave has been numerically reduced to avoid too fast oscillations of the field in time (central frequency ω_0 divided by 10). The side panels show different projections of this field, obtained by integrating $\text{Re}(E(x,y,t))$ along one of the three coordinates. **b–h**, Two-dimensional amplitude (**b–d**) and wrapped phase profiles (**e–g**) of the beam at three different frequencies, indicated on the beam spectrum (**h**). Lineouts of the unwrapped phase profiles along $y = 0$ are shown in the graphs below **e–g**. Note that the spatial wavefront at the central laser frequency ($\omega_0 = 800 \text{ nm}$) has been made perfectly flat by simulating the effect of an ideal deformable mirror, calculated at all frequencies of the beam (Supplementary Section II.A.4). This procedure removes achromatic spatial phase aberrations at all frequencies, leaving only chromatic aberrations in the phase maps of **e** and **f** (Supplementary Section II.A.4).

however, reveals a small frequency dependence of the wavefront tilt, in both spatial directions. We will now see how all these effects degrade the laser performances at focus.

To this end, we now calculate the two-dimensional Fourier-transform of $\tilde{E}(\omega, \mathbf{r})$ with respect to \mathbf{r} and thus determine the field $\hat{E}(\omega, \mathbf{k})$ that would be obtained in the focal plane of a perfect focusing optics. The intensity of this distribution is plotted in Fig. 5a, providing frequency-resolved focal spot profiles (see Supplementary Movie 3 for multiple perspectives). For comparison, Fig. 5b shows the same distribution in the case of a hypothetical perfect beam, with comparable integrated diameter and spectrum, but now free from STC. In this case, all frequencies are focused at the same location, with a focal spot of quasi-constant size.

In contrast, for the actual UHI100 laser beam, we observe that the exact position of the focal spot varies slightly with frequency³³ due to the frequency-dependent wavefront tilt observed in Fig. 4e–g. The evolution of the focal spot position is not purely linear with ω and occurs in both spatial directions. This effect can thus not be attributed simply to a residual PFT on the collimated beam (compare Fig. 5a and Fig. 2a), for example induced by a misalignment of the compressor, but has a more complex origin. In addition, on the red side of the spectrum, the focal spot is degraded and broadened, probably due to the crescent-shaped phase distortion observed in Fig. 4f,g for long wavelengths. Here again, this effect cannot be attributed to a basic residual coupling such as PFC (compare Fig. 5a and Fig. 2b).

This frequency dependence of the focal spot position and size has two consequences. First, it obviously increases the size of the global (that is, frequency-integrated) focal spot. Second, it reduces the effective local spectral bandwidth and thus tends to increase the pulse duration at focus. The first effect is illustrated in Fig. 5c,d, which compares projections of the focal spots of the real and

hypothetical ideal beams of Fig. 5a,b along two perpendicular directions. The size of the focal spot is increased by $\sim 25\%$ in both directions—a chromatic effect that can absolutely not be corrected by a standard adaptive optics system. The spatially integrated temporal intensity profile of the pulse can be calculated by using the spatiotemporal field $\hat{E}(t, \mathbf{k})$ at focus, obtained by Fourier transforming $\hat{E}(\omega, \mathbf{k})$ with respect to frequency (Supplementary Section II.B.1). This temporal profile is compared to that of the ideal beam in Fig. 5e, and an $\sim 25\%$ increase of the pulse duration due to STC is again observed.

Although these effects induced by residual STC may seem rather weak, their combination in three dimensions leads to a significant reduction of the peak intensity at focus, which should amount to $\varepsilon \approx (\tau \Delta x \Delta y)_{\text{meas}} / (\tau \Delta x \Delta y)_{\text{no STC}} \approx 0.75^3 \approx 0.42$. By comparing the peak values of $|\hat{E}(t, \mathbf{k})|^2$ for the measured and ideal beams, we can directly determine a ‘spatiotemporal Strehl ratio’ and indeed find $\varepsilon = 0.48$. In conclusion, due to the residual STC, this 100 TW laser of rather modest size by today’s standards can actually at best reach the peak intensities that would be obtained with a perfect 50 TW laser. Considering the curves of Fig. 2c,d, considerably more detrimental effects can be expected on PW-class lasers, showing the crucial need for spatiotemporal metrology for these systems.

Conclusions and outlook

We have obtained the first spatiotemporal characterization of a 100 TW peak power UHI laser. Our results indicate that such lasers can suffer from residual STCs, which are not as trivial as the simple pulse front distortions (PFT and PFC) usually expected on these systems. Such STCs had never been detected before due to the lack of suitable measurement techniques. Further investigations are needed to identify the origin of these couplings, which should make it possible to boost the effective performances of existing UHI lasers.

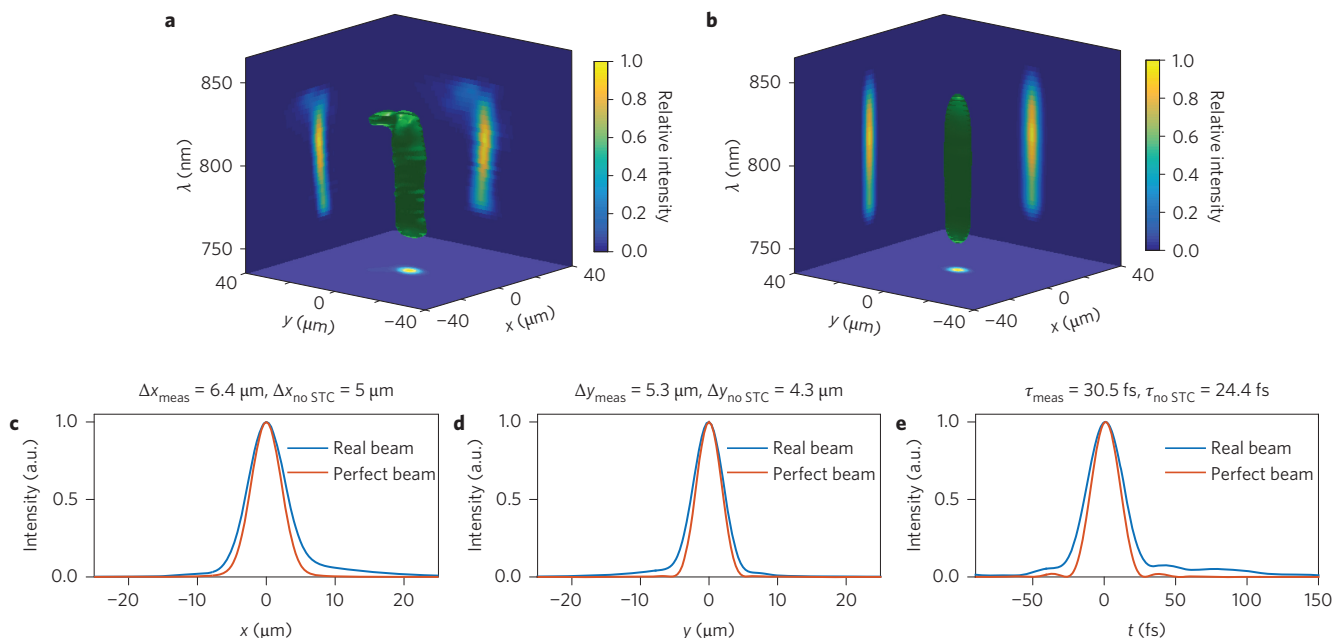


Figure 5 | Properties of the laser beam at focus. **a,b**, Spectrally resolved focal spot intensity profiles (isosurface at 5% of the peak value), respectively, for the measured UHI100 laser beam and for a hypothetical reference STC-free laser beam with the same diameter and spectrum before focusing. **c,d**, Comparison of projections of the spectrally (or temporally) integrated focal spots of these two beams along two perpendicular directions. **e**, Comparison of the the spatially integrated pulse temporal intensity profiles. All calculations have been carried out assuming a focal length of 250 mm (numerical aperture of the focused beam $\sim f/4$) for the focusing optics.

These results mark the beginning of a new era in the metrology of femtosecond laser beams, in particular for UHI lasers. From an engineering point of view, spatiotemporal metrology will be essential for the optimization of these facilities, especially in the PW power range, to guarantee that they actually deliver the expected peak intensities at focus. As far as UHI laser–plasma interactions are concerned, complete knowledge of the laser field in space and time at focus will provide crucial and long-awaited inputs for boundary conditions in numerical simulations with particle-in-cell codes. This will enable more reliable and realistic comparisons between experiments and simulations, and thus contribute to a better understanding of the physics involved and to the optimization of these experiments, in particular for the production of high-energy particle^{34,35} and X-ray beams^{36,37}. Finally, this new measurement capability is a prerequisite for the spatiotemporal shaping of UHI laser beams in order to engineer ‘structured’ laser fields and take advantage of the potential of STCs^{38,39} for the advanced control of relativistic motion of matter with light.

Received 3 March 2016; accepted 17 June 2016;
published online 25 July 2016

References

- Rullière, C. (ed.) *Femtosecond Laser Pulses* 2nd edn (Springer, 2007).
- Brabec, T. & Krausz, F. Intense few-cycle laser fields: frontiers of nonlinear optics. *Rev. Mod. Phys.* **72**, 545–591 (2000).
- Krausz, F. & Ivanov, M. Attosecond physics. *Rev. Mod. Phys.* **81**, 163–234 (2009).
- Chang, Z. *Fundamentals of Attosecond Optics* (CRC, 2011).
- Mourou, G. A., Tajima, T. & Bulanov, S. V. Optics in the relativistic regime. *Rev. Mod. Phys.* **78**, 309–371 (2006).
- Trebino, R. (ed.) *Frequency-Resolved Optical Gating: The Measurement of Ultrashort Laser Pulses* (Kluwer Academic, 2000).
- Walmsley, I. A. & Dorner, C. Characterization of ultrashort electromagnetic pulses. *Adv. Opt. Photon.* **1**, 308–437 (2009).
- Mairesse, Y. & Quéré, F. Frequency-resolved optical gating for complete reconstruction of attosecond bursts. *Phys. Rev. A* **71**, 011401 (2005).
- Akturk, S., Gu, X., Bowlan, P. & Trebino, R. Spatio-temporal couplings in ultrashort laser pulses. *J. Opt.* **12**, 093001 (2010).
- Bourasson-Bouchet, C., Stephens, M., de Rossi, S., Delmotte, F. & Chavel, P. Duration of ultrashort pulses in the presence of spatio-temporal coupling. *Opt. Express* **19**, 17357–17371 (2011).
- Kim, K. T. *et al.* Manipulation of quantum paths for space-time characterization of attosecond pulses. *Nature Phys.* **9**, 159–163 (2013).
- Bourasson-Bouchet, C., Mang, M. M., Delmotte, F., Chavel, P. & de Rossi, S. How to focus an attosecond pulse. *Opt. Express* **21**, 2506–2520 (2013).
- Strickland, D. & Mourou, G. Compression of amplified chirped optical pulses. *Opt. Commun.* **55**, 447–449 (1985).
- Trebino, R. *et al.* Simple devices for measuring complex ultrashort pulses. *Laser Photon. Rev.* **3**, 314–342 (2009).
- Gabolde, P. & Trebino, R. Single-shot measurement of the full spatio-temporal field of ultrashort pulses with multi-spectral digital holography. *Opt. Express* **14**, 11460–11467 (2006).
- Wyatt, A. S., Walmsley, I. A., Stibenz, G. & Steinmeyer, G. Sub-10 fs pulse characterization using spatially encoded arrangement for spectral phase interferometry for direct electric field reconstruction. *Opt. Lett.* **31**, 1914–1916 (2006).
- Bowlan, P., Gabolde, P. & Trebino, R. Directly measuring the spatio-temporal electric field of focusing ultrashort pulses. *Opt. Express* **15**, 10219–10230 (2007).
- Bragheri, F. *et al.* Complete retrieval of the field of ultrashort optical pulses using the angle-frequency spectrum. *Opt. Lett.* **33**, 2952–2954 (2008).
- Cousin, S. L., Bueno, J. M., Forget, N., Austin, D. R. & Biegert, J. Three-dimensional spatiotemporal pulse characterization with an acousto-optic pulse shaper and a Hartmann-Shack wavefront sensor. *Opt. Lett.* **37**, 3291–3293 (2012).
- Eilenberger, F., Brown, A., Minardi, S. & Pertsch, T. Imaging cross-correlation FROG: measuring ultrashort, complex, spatiotemporal fields. *Opt. Express* **21**, 25968–25976 (2013).
- Gallet, V., Kahaly, S., Govert, O. & Quéré, F. Dual spectral-band interferometry for spatio-temporal characterization of high-power femtosecond lasers. *Opt. Lett.* **39**, 4687–4690 (2014).
- Powell, D. Europe sets sights on lasers. *Nature* **14**, 264–265 (2013).
- Chu, Y. *et al.* High-contrast 2.0 petawatt Ti:sapphire laser system. *Opt. Express* **21**, 29231–29239 (2013).
- Sung, J. H., Lee, S. K., Yu, T. J., Jeong, T. M. & Lee, J. 0.1 Hz 1.0 PW Ti:sapphire laser. *Opt. Lett.* **35**, 3021–3023 (2010).
- Gaul, E. W. *et al.* Demonstration of a 1.1 petawatt laser based on a hybrid optical parametric chirped pulse amplification/mixed Nd:glass amplifier. *Appl. Opt.* **49**, 1676–1681 (2010).
- Miranda, M. *et al.* Spatiotemporal characterization of ultrashort laser pulses using spatially resolved Fourier transform spectrometry. *Opt. Lett.* **39**, 5142–5145 (2014).

27. Gallet, V. (ed.) *Dispositifs Expérimentaux pour la Caractérisation Spatio-Temporelle de Chaines Laser Femtosecondes Haute-Puissance* (Thèse de l'Univ. Paris XI, 2014).
28. Gallmann, L. *et al.* Spatially resolved amplitude and phase characterization of femtosecond optical pulses. *Opt. Lett.* **26**, 96–98 (2001).
29. Akturk, S., Gu, X., Gabolde, P. & Trebino, R. The general theory of first-order spatio-temporal distortions of Gaussian pulses and beams. *Opt. Express* **13**, 8642–8661 (2005).
30. Hebling, J. Derivation of the pulse front tilt caused by angular dispersion. *Opt. Quantum Electron.* **28**, 1759–1763 (1996).
31. Bor, Z. Distortion of femtosecond laser pulses in lenses. *Opt. Lett.* **14**, 119–121 (1989).
32. Moulet, A., Grabielle, S., Cornaggia, C., Forget, N. & Oksenhendler, T. Single-shot, high-dynamic-range measurement of sub-15 fs pulses by self-referenced spectral interferometry. *Opt. Lett.* **35**, 3856–3858 (2010).
33. Kahaly, S. *et al.* Investigation of amplitude spatio-temporal couplings at the focus of a 100 TW–25 fs laser. *Appl. Phys. Lett.* **104**, 054103 (2014).
34. Esarey, E., Schroeder, C. B. & Leemans, W. P. Physics of laser-driven plasma-based electron accelerators. *Rev. Mod. Phys.* **81**, 1229–1285 (2009).
35. Macchi, A., Borghesi, M. & Passoni, M. Ion acceleration by superintense laser-plasma interaction. *Rev. Mod. Phys.* **85**, 751–793 (2013).
36. Teubner, U. & Gibbon, P. High-order harmonics from laser-irradiated plasma surfaces. *Rev. Mod. Phys.* **81**, 445–479 (2009).
37. Thaury, C. & Quéré, F. High-order harmonic and attosecond pulse generation on plasma mirrors: basic mechanisms. *J. Phys. B* **43**, 213001 (2010).
38. Vincenti, H. & Quéré, F. Attosecond lighthouses: how to use spatiotemporally coupled light fields to generate isolated attosecond pulses. *Phys. Rev. Lett.* **108**, 113904 (2012).
39. Pariente, G. & Quéré, F. Spatio-temporal light springs: extended encoding of orbital angular momentum in ultrashort pulses. *Opt. Lett.* **40**, 2037–2040 (2015).

Acknowledgements

The authors thank P. d'Oliveira, F. Réau, C. Pothier and D. Garzella for operating the UHI100 laser source. The research leading to these results has received funding from the European Research Council (ERC grant agreements nos 240013 and 334948). A.B. acknowledges support from the Marie Curie Fellowship EU-FP7-IEF-ALPINE (627856) and G.P. IDEX Paris Saclay for his PhD grant.

Author contributions

G.P., V.G. and F.Q. developed the TERMITES technique. G.P. and V.G. built the experimental set-up and G.P. developed the data processing program and analysis/visualization tools with initial contributions from V.G. The measurements were performed and analysed by G.P. and A.B. F.Q. and O.G. supervised the overall work.

Additional information

Supplementary information is available in the online version of the paper. Reprints and permissions information is available online at www.nature.com/reprints. Correspondence and requests for materials should be addressed to F.Q.

Competing financial interests

The authors declare no competing financial interests.